Economic and environmental assessment of a CO_2 solar-powered plant with packed-bed thermal energy storage

Battisti, F. G.; de Araujo Passos, L. A.; da Silva, A. K.

DOI
10.1016/j.apenergy.2022.118913

Publication date
2022

Document Version
Final published version

Published in
Applied Energy

Applied Energy 314 (2022) 118913

Contents lists available at ScienceDirect

Applied Energy

journal homepage: www.elsevier.com/locate/apenergy

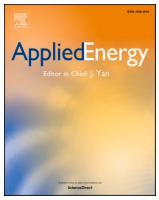

Economic and environmental assessment of a CO_2 solar-powered plant with packed-bed thermal energy storage

F.G. Battisti [a], L.A. de Araujo Passos [b], A.K. da Silva [a,*]

[a] Department of Mechanical Engineering, Federal University of Santa Catarina, Florianópolis, SC 88040-900, Brazil
[b] Delft Center for Systems and Control, Delft University of Technology, Delft 2628 CD, Netherlands

ARTICLE INFO

Keywords:
Supercritical carbon dioxide
Concentrated solar power plants
Thermal energy storage
Environmental impact
Levelized cost of energy (LCOE)

ABSTRACT

Investigating supercritical natural fluids for efficient and clean energy production has become a trending research topic due to their technical and environmental advantages. However, on account of the supercritical operational conditions, using specially-developed components increases manufacturing prices, especially when dealing with solar-powered plants assisted by thermal energy storage (TES) systems. This paper assesses the economic and environmental trends of an integrated supercritical carbon dioxide (s-CO_2) solar-powered plant. The system is composed of a packed-bed TES system, a solar field, and a power block while considering conventional backup heating. Transient year-around numerical simulations explore several operational conditions relying on detailed cost and typical meteorological year (TMY) data. Also, the modeling accounts for the system's environmental sustainability through a penalization cost regarding CO_2 emissions due to auxiliary heating. With parametric analyses, the study assesses the compromise solutions minimizing the levelized cost of energy (LCOE). The results revealed the possible feasibility of the integrated system using such a TES technology for s-CO_2 and evidenced several venues for further examination. In the end, a sensitivity analysis investigates the influence of the specific costs and TMY data on the LCOE.

1. Introduction

When dealing with solar-powered plants, using thermal energy storage (TES) technologies is undoubtedly one of the key aspects for increasing energy dispatchability while boosting the solar fraction of energy deployed [1,2]. In this sense, thermocline packed-bed and two-tank molten salt systems are two technologies commonly used in commercial applications of conventional concentrated solar power (CSP) plants [3–5]. Because of the proven reliability of both TES technologies, innovative power systems continue to assess them, which is the case of plants using supercritical carbon dioxide (s-CO_2) as heat transfer fluid (HTF) [6–8]. Moreover, s-CO_2 stands out technically and environmentally amongst other next-generation working fluids [9–13].

Arguably, packed-bed TES is a more efficient and compact option since the HTF and the storage medium are in direct contact within a single tank. However, the high-pressure and high-temperature levels required in s-CO_2-based plants might significantly increase the manufacturing costs of packed-bed systems given the need for special alloys and mechanically robust walls [14–16]. On the other hand, two-tank TES systems require large volumes for the storage medium, i.e., molten salts, at different temperature levels and an additional heat exchanger, which inherently decreases the system efficiency. Also, the operational limits of such salts constrain the set of allowable working temperatures [17]. Although TES systems can increase the dispatchability of power plants and reduce auxiliary heating power, they usually add to a large extent the overall cost of such installations. Furthermore, from an environmental standpoint, reducing conventional fossil-based supplementary heating is recommended. The challenge, therefore, is to appropriately match performance and expenses to overcome constraints related to s-CO_2 TES-aided systems.

The current literature provides some insight into TES systems and s-CO_2 solar-powered plants. For instance, Ref. [18] suggested that packed-beds are technically feasible for a CSP plant running with s-CO_2. Nonetheless, the high operational pressure considered substantially raised the costs turning it in one of the main limitations for such technology. Integrating a packed-bed with an s-CO_2 power cycle was thermo-economically investigated by Refs. [19,20], but considering indirect heating and using air as HTF for the TES device and solar field. In Ref. [21], an s-CO_2-based packed-bed had its exergetic efficiency

* Corresponding author.
E-mail address: a.kupka@ufsc.br (A.K. da Silva).

https://doi.org/10.1016/j.apenergy.2022.118913
Received 11 January 2021; Received in revised form 17 June 2021; Accepted 6 March 2022
Available online 21 March 2022

Nomenclature

A	Area [m^2]
b	Iteration counter [–], specific cost [US$/(kg, J or MWh)]
C	Constant [–], Cost [US$]
c	Mass-specific heat at constant pressure [J/(kg•°C)]
D	Diameter [m]
DNI	Direct normal irradiation [W/m^2]
d	Particle (sphere) diameter [mm]
e	Mass-specific energy [J/kg]
$\dot{E}$	Thermal power transfer [W]
h	Volumetric convective heat transfer coefficient [W/(m^3• °C)]
i	Mass-specific enthalpy [J/kg]
j	Given time step, counter [–]
k	Thermal conductivity [W/(m• °C)], indexer [–]
L	Length [m]
m	Mass [kg]
$\dot{m}$	Mass flow rate [kg/s]
P	Pressure [MPa]
T	Temperature [°C]
t	Time [s] or Thickness [m]
U	Tip speed [m/s]
u	Velocity [m/s]
V	Volume [m^3]
$\dot{W}$	Power [W]
z	Axial distance [m]
dr	Discount rate [%]
LT	Lifetime [a]
UA	Global conductance [W/K]
W	Energy produced/consumed [J]

Subscripts and superscripts

0	Previous time step or reference value
$1, 2, \ldots$	Counters
α	Equation generic subindex
a	Approximated
b	Iteration counter or Indexer
C	Compressor, charging
Coll	Collector
E	East node
e	East interface
eff	Effective
EG	Electric generator
F	Fluid
$High$	High
i	Insulation, indexer
In	Inlet
j	Indexer
k	Indexer
Lid	Lid
Max	Maximal
Net	Net
NG	Natural gas
Opt	Optimal
Out	Outlet
P	Current node
PB	Power block
$Pump$	Pump, compressor
Rec	Receiver
ref	Reference
S	Solid
s	Isentropic
st	Steel
Sto	Stored
T	Turbine
v	Volumetric
W	West node
w	West interface
$Wall$	Wall
z	Axial direction
*	Normalized
Air	Air
Aux	Auxiliary
Aper	Aperture
Bypass	Bypass
Ele	Electric
Env	Environmental
Equip	Equipment
Low	Low
Mirrors	Mirrors
MO	Maintenance and operation
Site	Site
SF	Solar field
Sys	System
TES	Thermal energy storage system

Greek symbols

β	Isobaric expansion coefficient [1/K]
Γ	Distance to the origin point [–]
Δ	Difference, increment, step
ε	Porosity [–]
φ	Given arbitrary quantity
η	Efficiency [–]
θ	Incidence angle [–]
κ	Isothermal compressibility coefficient [1/Pa]
ρ	Volume-specific mass [kg/m^3]
σ	Yield strength [MPa]
ϕ	Dimensionless mass flow rate [–]
χ	Correction parameter [–]
ω	Shaft speed ratio [–]

Abbreviations

Co	Cooler
CSP	Concentrating solar power
EG	Electric generator
HTF	Heat transfer fluid
HTR	High-temperature recuperators
LTR	Low-temperature recuperators
LHV	Lower heating value
LMTD	Logarithmic mean temperature difference
MC	Main compressor
PCHE	Printed circuit heat exchanger
RC	Recompression compressor
s-CO_2	Supercritical carbon dioxide
T	Turbine

Miscellaneous

$\bar{}$	Averaged value
$\langle\,\rangle$	Time-averaged value
$\rightarrow$	Vector designator

analyzed over cycles of charge and discharge, which pointed out thermal dispersion and heat losses as the leading sources of irreversibility. Other studies have explored different TES technologies. For instance, some authors considered molten salts [22,23] and granite [24] TES tanks to deal with solar input oscillations in s-CO_2 systems heated indirectly. Ref. [25] compared several s-CO_2-based solar-powered cycle configurations relying on a two-tank TES solution. Like Ref. [26], which investigated the short- and long-term performance of a recompression CO_2 power cycle with a two-tank storage, other works also considered off-design modeling for evaluating the annual performance of a central-collector plant with TES alternatives, e.g., Ref. [27]. Ref. [28] used a TES system composed of concrete concentric tubes while investigating the s-CO_2 power plant dynamics and mass inventory control. Also, some authors suggested s-CO_2 as the storage medium [29] and a novel TES system combining an ejector condensing cycle [30].

Despite that a few theoretical studies addressed the use of TES solutions for s-CO_2-based plants, these do not provide sufficient information on designing and minimizing inherent costs for such systems, i.e., highlighting optimal design and operation parameters and the system integration. Ref. [31] presented a thermo-economic analysis of an indirect s-CO_2 cycle with a two-tank TES system. Considering a molten salt power tower, Ref. [32] optimized an s-CO_2 power cycle minimizing the levelized cost of energy (LCOE). Moreover, Ref. [33] performed an economic-environmental multi-objective optimization of a molten salt indirect s-CO_2 cycle with two-tank TES system. However, none of them evaluated a direct configuration using a packed bed TES system. The present authors have previously modeled and investigated design trends of a packed-bed TES running with s-CO_2 in Ref. [34]. Although the study investigated several technical aspects, it did not assess economic or environmental elements nor considered an auxiliary heating system.

Therefore, given the relevance of the cost of packed-bed TES systems for s-CO_2 applications, this study aims to analyze the economic trends of an integrated system composed of such a TES option, a solar field, and a power block while considering s-CO_2 as HTF and conventional auxiliary heating as a backup. Transient year-around numerical simulations explore several operational conditions regarding detailed costs and typical meteorological year (TMY) data for a reference city on CSP applications, i.e., Daggett/USA. In addition, the modeling accounts for the system's environmental sustainability through a penalization cost regarding CO_2 emissions due to the backup heater. The results show that the size of the TES system, the required auxiliary heating, and the related costs all depend on the operational conditions. Through parametric analyses, the study assesses compromise solutions seeking to minimize the LCOE. In the end, a sensitivity analysis investigates the influence of the specific costs and TMY data on the LCOE.

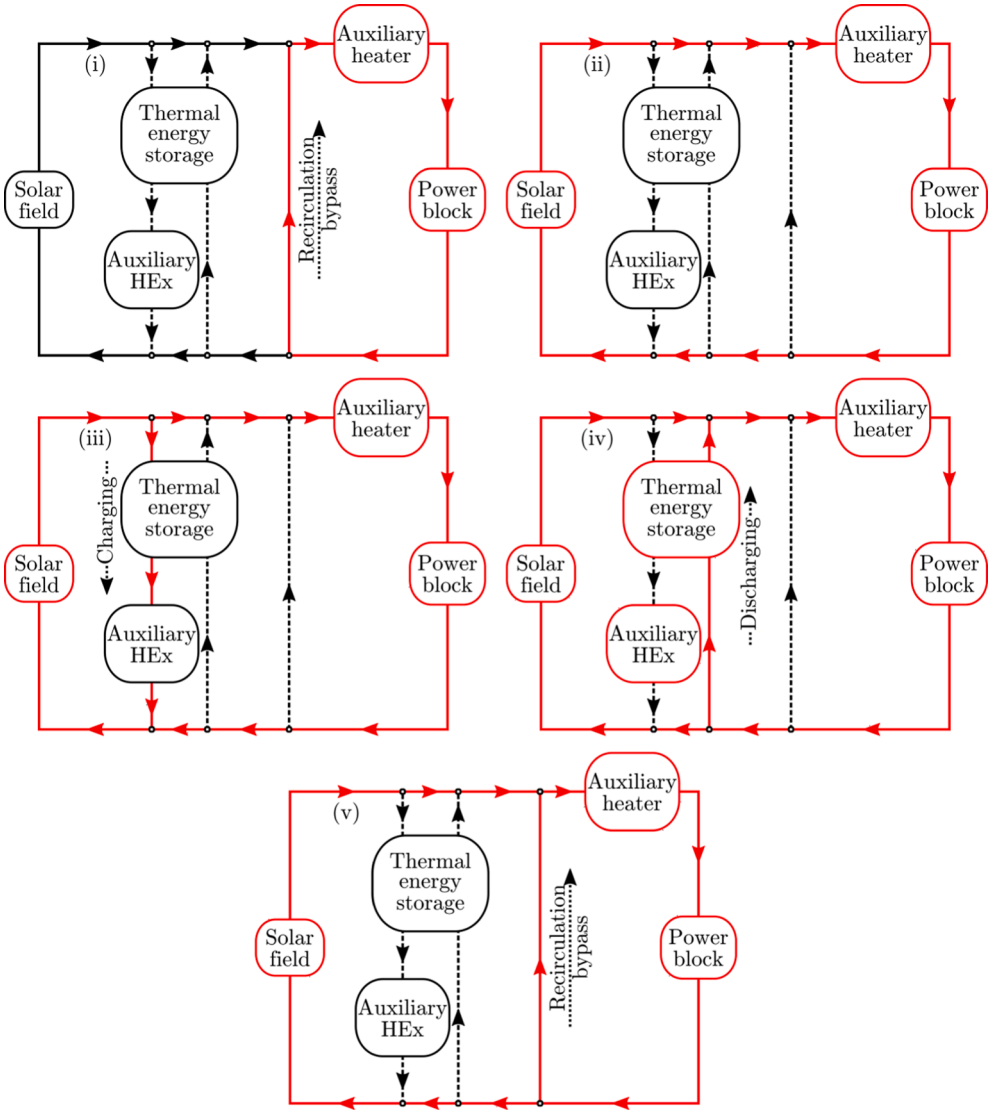

Fig. 1. Integrated system's layout and its operation strategies: (i) disregarding solar field and TES system; (ii) with the solar field providing the design mass flow rate; (iii) surplus of mass flow rate from the solar field being directed to charging the TES system; (iv) lacking mass flow rate from the solar field being retrieved from discharging the TES system; and (v) lacking mass flow rate from the solar field and discharging of the TES system not being possible, so the recirculation bypass engages the auxiliary heater directly.

2. Methodology for the system modeling

The following subsections present the methodology employed for system modeling and evaluation. Section 2.1 describes the integrated system and its numerical routine, whereas Sections 2.2, 2.3, and 2.4 present the models considered for simulating the power block, the solar field, and the packed-bed TES systems, respectively. Additionally, Section 2.5 presents the approach for the system economics assessment. Moreover, all numerical routines were implemented in MATLAB [35] using fluids properties from CoolProp [36,37]. Previous works already validated the overall modeling used for the solar field, packed-bed TES, and power block.

2.1. Integrated system and its numerical routine

Fig. 1 presents the overall schematics of the integrated s-CO_2 system considered in this study and its operational strategies, which will be presented in detail. For the power block, high-temperature s-CO_2 solar-powered plants already considered several Brayton cycle configurations, including re-heating, recompression, and intercooling [9]. Nevertheless, recuperative and recompression cycles may be considered satisfactory in terms of performance-relative costs since further increasing the configuration complexity seems not to directly translate into a relative performance upgrade. Therefore because the cycle enhancement is not the main focus of analysis, the power block of the present study shown in Fig. 2 operates as a conventional s-CO_2 recompression Brayton cycle, which is a highly-ranked configuration for solar-powered plants [38,39]. Moreover, the power block design has a nominal net power production output of 10 MW while being assisted by a conventional backup heater using natural gas as fuel. Such an auxiliary subsystem ensures the power block inlet condition at all times; hence, it operates in steady state regardless of the solar gain.

The solar power input is accounted for through parabolic trough collectors (i.e., the solar field in Fig. 1), which have been tested with s-CO_2 and have valuable experimental data for theoretical modeling and verification [40]. For extending the power production while still relying on the solar source beyond its direct availability, a packed-bed TES system is responsible for storing (charging) and releasing (discharging) the surplus of thermal power from the solar field. Fig. 3 shows a schematic representation of a single TES device employed. Although TES devices and solar collectors are inherently more expensive than conventional fossil-based heating, such systems enhance the environmental sustainability of the power plant by reducing its CO_2 emissions. At this point, it is worth recalling that specific optimization of the packed-bed TES devices for s-CO_2-based CSP generation is a major feature still requiring further investigation. Specifically, such systems may be more efficient than two-tank devices, but the working pressures required by the HTF might impair their economic feasibility [18]. Also, following Ref. [34], the packed-bed TES device considered includes auxiliary

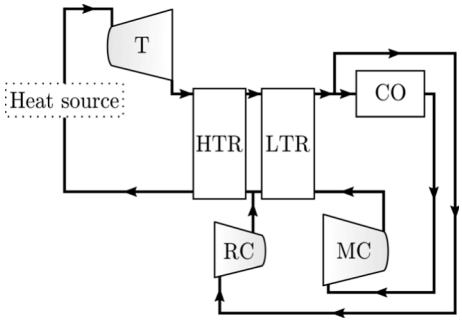

Fig. 2. A heat source-dependent recompression Brayton cycle composed of a turbine (T), main (MC) and recompression (RC) compressors, a cooler (CO), and low and high-temperature recuperators (LTR and HTR, respectively).

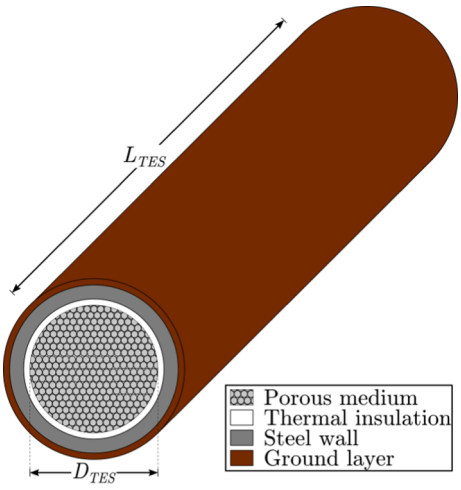

Fig. 3. Schematic representation of the in-ground cylindrical packed-bed TES device characterized by the diameter D_{TES} and length L_{TES}, with alumina spheres composing the porous medium.

compressors at each end for recirculating the HTF (i.e., for reestablishing the pressure levels), which were omitted in this graphic representation.

As shown in Fig. 1, the parallel disposition between solar field, TES system, and power block (with the auxiliary heater between the TES system and the power block) allows different dynamic operation strategies. These alternatives are described in detail next and shown in the five subplots of Fig. 1, in which red-continuous lines indicate active flow, whereas black dotted lines indicate inactive paths.

First, the simplest strategy (i) disregards both the solar field and the TES system, i.e., the system runs through the recirculation bypass with the auxiliary heater as the energy source for the power block. Then, other system strategies emerge from the solar field being able to act as the heat source. If the solar field provides a mass flow rate equal to the power block design value, the system disregards the TES device, and the HTF flows through the auxiliary heater to the power block (ii). If the solar collectors provide a mass flow rate higher than the power block design value, the system splits the HTF flow; hence, the power block receives the design value while the remaining fraction flows to the TES for storing the surplus thermal energy (iii).

If the solar field provides a mass flow rate lesser than the power block design value, the system assesses the possibility of discharging the TES with the missing mass flow rate (iv). On the other hand, if such a process is unavailable, the system uses the recirculation bypass and auxiliary heater (v). Moreover, if the solar field cannot act as the heat source, the system follows either one of the strategies just discussed but now considering all the mass flow rate instead of just a fraction of it.

Furthermore, when the heat gain from the solar field is excessive within a system time step (i.e., when the solar collector could provide a surplus of mass flow rate) and if charging the TES device is unavailable (i.e., it is thermally loaded), the system control defocuses the solar field. With such a common practice, the rejection of thermal power surplus enables the controlled mass flow rate to equal the power block design value.

For easing the numerical simulations, in the current modeling, an auxiliary heat exchanger was included at the charging outlet of the TES system (see “Auxiliary HEx” in Fig. 1) for heating or cooling the mass flow rate leaving the TES system during the charging, in order to maintain its temperature always equal to that of the mass flow rate exiting the power block. The inclusion of this auxiliary heat exchanger was necessary for assuring the inlet condition to the solar field remains at design condition throughout all time steps of all simulations as further discussed in Section 2.3. This boundary condition allows for the annual economic assessment to be performed in a time-efficient manner by

avoiding the numerical iteration between the solar field and the TES device within a system time step. Although real plants would not use such a component, its inclusion becomes acceptable since it significantly reduces the simulation time. Thus, an active overall controller would consider the solar field-TES system interaction. Furthermore, all the energy used by the auxiliary heat exchanger for heating the HTF adds to the total backup heating. On the other hand, the routine disregards the energy from cooling the HTF lost to the environment. Such a strategy is similar to what happens with the solar gain when the solar field efficiency decreases with the increase of its HTF inlet temperature.

The numerical routine runs the integrated system on an annual basis, following the discussion above. The flowchart in Fig. 4 summarizes the overall system control strategy. For all the simulations performed, the system time step is $\Delta t_{Sys} = 1$ h, i.e., the resolution of the TMY data used. Moreover, from mesh independence studies, the TES device time step is $\Delta t_{TES} = 60$ s, and the TES axial discretization is $N_z = 160$. For a given set of input parameters and variables values (i.e., see Section 2.4), the routine starts at $t_{Sys} = 1$ h $= \Delta t_{Sys} = 1$ h by evaluating the solar field availability. Then, the control scheme decides for TES charging (light blue background), TES discharging (light red background), or straight auxiliary heating based on the outlet temperature for a TES time step of $\Delta t_{TES} = 60$ s. Also, although the numerical routines developed can account for short-term perturbations like in Ref. [26], the hourly resolution of the TMY data diminishes their influence on the system's performance. Hence, for enabling less computationally expensive modeling, the overall system does not consider such perturbations in detail.

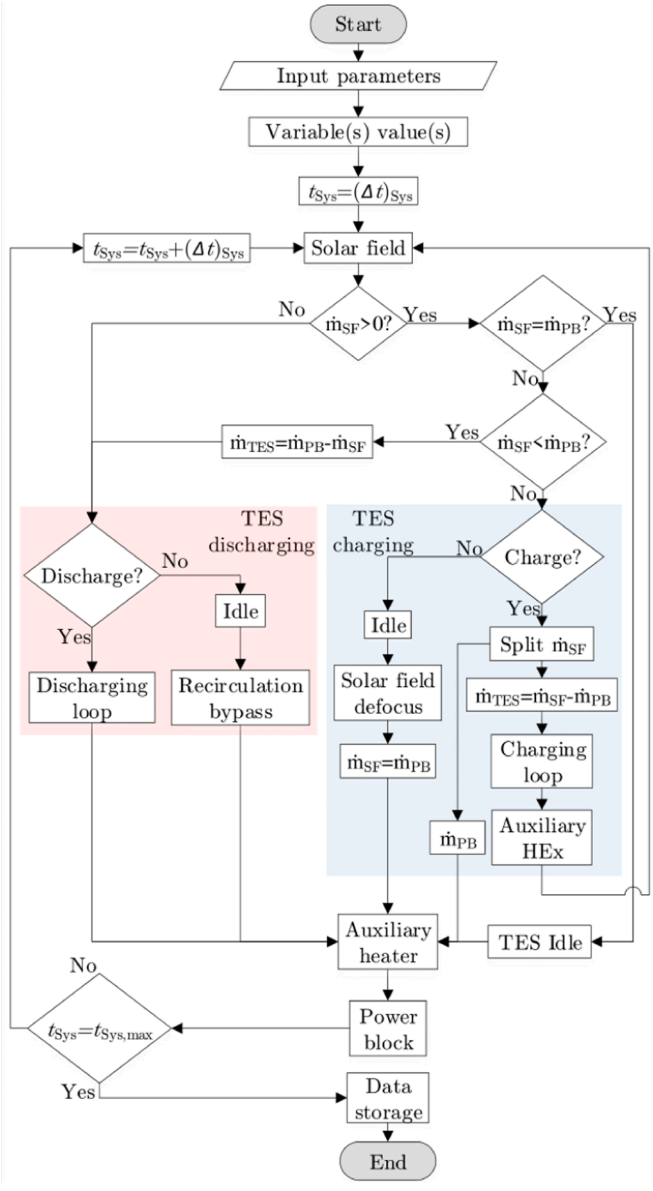

Fig. 4. Flowchart of the main numerical routine with TES charging and discharging processes following the operations strategies of Fig. 1.

2.2. Power block

As shown in Fig. 2, the power block is composed of a turbine (T), main (MC) and recompression (RC) compressors, a cooler (CO), and low and high-temperature recuperators (LTR and HTR, respectively). Depending on the operation strategy, as already discussed along with Fig. 1, the heat source may be the solar field, the TES system, the auxiliary heater, or a combination of these.

The modeling of the power block employs the methodology of Ref. [41] for s-CO_2 recompression Brayton cycles. More specifically, the turbomachinery rely on the modeling of Ref. [42], which uses experimentally-validated efficiency performance maps. The compressor model requires adjusted isentropic values of the enthalpy change and efficiency as [41,42]

$$\Delta i_{C,s} = \frac{\chi_1 U^2}{\omega^{(20\phi)^3}} \quad \text{and} \quad \eta_C = C\frac{\chi_2}{\omega^{(20\phi)^5}}\eta_{C,0}\,, \tag{1}$$

for which i is the mass-specific enthalpy, ω the shaft speed ratio, U is the tip speed, and $\eta_{C,0}$ the reference efficiency. The correction parameters χ_1 and χ_2 are fourth-order polynomials, which are functions of the dimensionless mass flow rate [41,42]

$$\phi = \frac{\dot{m}}{\rho U D_C^2}\left(\frac{1}{\omega}\right)^{0.2}, \tag{2}$$

for which $\dot{m}$ is the mass flow rate, ρ the volume-specific mass, and D_C the rotor diameter. Moreover, the turbine model determines the mass flow rate and the device isentropic efficiency as [41,42]

$$\dot{m} = \rho\left(2\Delta i_{T,s}\right)^{0.5} A_T \quad \text{and} \quad \eta_T = 2\left[\frac{U}{\left(2\Delta i_{T,s}\right)^{0.5}}\left(1-\frac{U^2}{2\Delta i_{T,s}}\right)^{0.5}\right]\eta_{T,0}\,, \tag{3}$$

for which $\eta_{T,0}$ is the reference efficiency and $\Delta h_{T,s}$ the turbine isentropic enthalpy change. Additionally, the model for the recuperators considers them as counterflow printed circuit heat exchangers (PCHE), following the geometry presented by Ref. [43]. The discretized approach considers energy balances for each fluid and the solid layer between them. The heat exchangers consider pressure drops [42] and utilize the Gnielinski's correlation [44] for the heat transfer coefficients, as discussed by Ref. [41]. Furthermore, it is worth mentioning that different authors (e.g., Refs. [45,46]) already considered similar power block modeling approaches. For the sake of conciseness, for further details, refer to the complete formulations of Refs. [41,42].

Focusing on the particular selected input parameters, for the 10 MW net power production set as the design target, the power block input data set considers an inlet (i.e., high-end or upstream the turbine) temperature of $T_{PB,In} = 550$ °C and main compressor inlet temperature and pressure of 50 °C and $P_{PB}^{Low} = 10$ MPa, respectively. Following Ref. [42], for the recompression stage, the optimal mass flow rate split fraction of 25.8% maximizes the cycle efficiency. With such parameters, the power block model outputs a high-temperature-end pressure of $P_{PB}^{High} = 25$ MPa, a mass flow rate of $\dot{m}_{PB} = 133.2$ kg/s, a power block outlet temperature of $T_{PB,Out} = 407.42$ °C and a net power output of $\dot{W}_{PB}^{Net} = 9.93$ MW ~ 10 MW.

The high operation pressure required by s-CO_2 systems remains the main challenge for the application of such a fluid. The value of 25 MPa

for the high-temperature-end pressure may represent a limitation for the present system. Nonetheless, researchers are currently investigating equipment and materials for withstanding high-temperature and high-pressure conditions. Additionally, future works should consider alternative configurations as suggested by Ref. [47], in which the heat supply to the power block occurs at the low-end pressure.

2.3. Solar field

For the solar field, the modeling of Refs. [26,41] is employed. The solar heat gain in the solar collector field is calculated using the thermal performance reported for a parabolic trough field, whose efficiency depends on the average temperature of the absorber. For the time-dependent collector outlet temperature, the efficiency is calculated based on the LS-2 geometry and heat transfer mechanics reported in Ref. [48]. Thus, the energy balance in the absorber is expressed as [41]

$$m_{Coll}c_{Coll}\frac{dT_{Coll}}{dt} = \eta_{Coll}DNI\cos(\theta)\left(\frac{A_{Aper}}{N_{Coll}}\right) + 2\dot{m}_F c_F\left(T_{F,In} - T_F\right), \quad (4)$$

where m is the mass, c the mass-specific heat at constant pressure, T the temperature, t the time, η the overall efficiency, DNI the direct normal irradiation, θ the angle of incidence (details regarding its calculation are shown in Ref. [48]), A the area, and N_{Coll} the number of independent parallel collector rows. The subscripts $Coll$, $Aper$, F, and In refer to a parabolic trough collector, total solar field aperture area of mirrors, the HTF, and inlet, respectively. In Eq. (4), the LHS represents the energy stored within the absorber, the first term in the RHS represents the overall solar energy input, and the second term in the RHS refers to the thermal transfer to the HTF. In this study, the solar field is split into $N_{Coll} = 100$. Moreover, the total solar field aperture area of mirrors is obtained as

$$A_{Aper} = SM \cdot A_{SF,ref}, \quad (5)$$

where SM is the solar multiple and $A_{SF,ref}$ the reference solar field aperture area. The $A_{SF,ref}$ value definition was determined such that the solar field would provide a total mass flow rate equal to that required by the power block, i.e., $\dot{m}_{PB} = 133.2$ kg/s, while observing the HTF outlet temperature to be equal to $T_{PB,In} = 550$ °C. Then, assuming the reference conditions of solar normal radiation of 900 W/m^2, air temperature of 20 °C, no wind, and HTF inlet temperature of $T_{PB,Out} = 407.42$ °C, the value of $A_{SF,ref} = 435.5$ m^2 was determined. For more detailed information on the modeling employed for the solar collectors, one may refer to Refs. [26,41].

Although $P_{PB}^{High} = 25$ MPa may be a high operating pressure for conventional solar trough collectors, the optimal performance of the solar collector at the target temperature set requires that specific condition. Such a condition is possibly the main constraint for the collectors, which are susceptible to mechanical failures, such as leaking. Nonetheless, the value obtained from the power block modeling was employed for the sake of fairness. For assessing the system appropriately and enabling further comparisons, the simulations require the best condition for the power block, i.e., its optimal performance. If the simulations used lower values of high-end temperature and pressure, the sub-optimal operation of the power block could impair the analyses. Then, operating at a non-optimal condition is not satisfactory. Furthermore, considering the high operation pressure as a possible limitation for the system, future studies should address the topic investigating the development of new equipment and materials, for instance.

All analyses used the DNI, air temperature (T_{Air}), and wind speed (u_{Air}) data for Daggett/USA as inputs, which is a reference city on CSP applications. Similar to Ref. [26], the TMY basis of Ref. [49] provided such data, which are shown graphically by the 8760 black dots in each plot of Fig. 5 – each dot represents one hour of the year. Furthermore, the solar field modeling and the TMY data were used for obtaining the

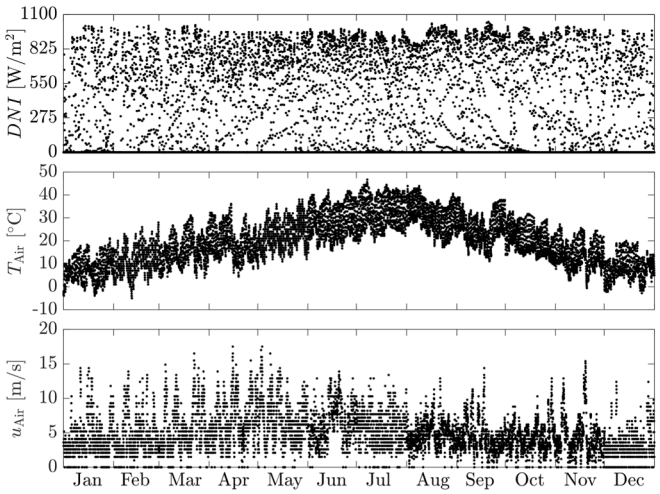

Fig. 5. Graphic representation of the Typical Meteorological Year (TMY) data for Daggett/USA from Ref. [49]: direct normal irradiation (DNI), air temperature (T_{Air}), and wind speed (u_{Air}).

CSP HTF outlet temperature and mass flow rate for each hour of the year considering that the HTF always entered the solar field at $T_{PB,Out} = 407.42$ °C and $P_{PB}^{High} = 25$ MPa, as previously mentioned. Then, for each SM value investigated, the solar field annual outputs were obtained by optimizing the mass flow rate so that $T_{SF,Out}$ would be as close as possible to $T_{PB,In} = 550$ °C. Therefore, intending to exam a broad range of inputs, this procedure was observed for SM values of 1.5, 2.0, 2.5, 3.0, 3.5, and 4.0.

2.4. Packed-bed TES system

The numerical model utilized for evaluating the performance of the packed-bed TES system in this study follows Ref. [34]. As shown schematically in Fig. 3, a single TES device consists of an in-ground tank characterized by the diameter D_{TES} and length L_{TES}, with alumina spheres of diameter d composing the packed-bed whose porosity was fixed at $\varepsilon = 0.35$.

The core numerical model is axisymmetric and uniformly axially discretized, which uses a two-temperature formulation, i.e., one for the alumina spheres (porous medium) and another for the s-CO_2 (fluid). Appx. A provides the general expressions of the energy conservation equations for the fluid and solid phases within the packed bed. With this modeling, the thermal capacitances, pressure drop, and the fluid variable thermophysical properties are taken into account while predicting realistic dynamic behaviors. Ref. [34] provides further information and details on the packed-bed modeling, which go beyond the scope of the present work. Furthermore, aiming to better account for the thermal losses, following the indications of Ref. [50], instead of a fixed value for the ground temperature, this was considered as 3 °C above the air temperature at each system time step.

Additionally, for all time steps when the TES device idles, i.e., when it is not being charged or discharged, the numerical routine follows the procedure described in Ref. [34], except for the improvements detailed in Appx. B. Briefly, during idle, the pressure field becomes spatially uniform, but still time-dependent; then, the pressure value for each time step is numerically obtained regarding that the fluid total mass within the TES must remain constant while heat is exchanged between fluid and porous medium as well as lost to the surroundings.

From an energy balance between the solid releasing and the fluid receiving thermal power, the sizing of the total TES volume is obtained as a function of the selected number of storage hours (t_{TES}) as

$$V_{TES,Total} = \frac{\dot{m}_{PB}\left[i_F\left(T_{PB,In}, P_{PB}\right) - i_F\left(T_{PB,Out}, P_{PB}\right)\right]t_{TES}}{(1-\varepsilon)\rho_S \bar{c}_S 0.8\left(T_{PB,In} - T_{PB,Out}\right)}, \quad (6)$$

for which i_F is the fluid mass-specific enthalpy as a function of temperature and pressure, $\varepsilon = 0.35$ the porosity, $\rho_S \approx 3950$ kg/m^3 and $\bar{c}_S \approx 1150$ J/(kg K) the particles volume-specific mass and average mass-specific heat at constant pressure, respectively [34]. For design, the solid axially-averaged temperature difference was considered as 80% of the inlet and outlet power block temperature difference, and it was assumed that the time-averaged thermal power released by the solid equals the power required for taking the power block mass flow rate $\dot{m}_{PB}$ from the outlet to the inlet power block conditions. Moreover, using Eq. (6), the length for each cylindrical TES device is given by

$$L_{TES} = \frac{4V_{TES,Total}}{\pi D_{TES}^2 N_{TES}}, \quad (7)$$

with which the L_{TES} values shown in Table 1 are obtained for various N_{TES}, t_{TES}, and D_{TES}.

Including the parameter N_{TES} in the study intends to deal with the possibly large pressure drops related to higher mass flow rates flowing through the porous medium structure of the packed bed. Hence, the charging or discharging mass flow rate is equally divided between the N_{TES} packed-bed TES devices. Also, because all TES devices are equal and subjected to the same inputs and boundary conditions, just one is simulated, and its response is replicated for all the remaining. Moreover, since the TES simulation uses a much smaller time step than that of the integrated system, for easing the further calculations, the TES outlet mass flow rate and mass-specific enthalpy are obtained as temporal averages for each system time step. Also, the power spent with the auxiliary compressors adds to the outlet fluid flow through energy balances, i.e., it contributes to the actual outlet enthalpy.

2.5. System economics

The economic assessment of the integrated CSP plant evaluates the costs of the main equipment composing of the three major subsystems, i.e., solar field, TES system, and power block. Based on the literature (e.g., Refs. [51,52]), the widely-regarded approach of using scalable functions was chosen. This method indicates that the costs for different sizes of components are related to references cases previously determined following an expression similar to

$$\frac{C}{C_{ref}} = \left(\frac{S}{S_{ref}}\right)^n, \quad (8)$$

where C is the cost, S a metric for the equipment size, n the scaling exponent, and the subscript *ref* refers to the reference case. Therefore, the costs of manufacturing the subsystems within the power block may be estimated relying on reference data for s-CO_2 [53]. Additionally, Eq. (8) may also be used for estimating the costs for the solar field and the auxiliary heating process. Table 2 presents the expressions used for determining the equipment costs for the power block and the solar field.

Therefore, for the power block considered in Fig. 2, using the expressions from Table 2, the cost is estimated as

$$C_{PB} = C_T + C_{MC} + C_{RC} + C_{HTR} + C_{LTR} + C_{Co} + C_{EG}, \quad (9)$$

which also includes an electric generator (C_{EG}). The costs of the turbine and compressors are estimated based on the power produced/consumed per each, which are determined by the mass flow rate through and the inlet-outlet enthalpy difference of each one. For the recuperators, the costs are estimated based on the global conductance, which is obtained using discretization (into N sub-heat exchangers), considering the total thermal power transferred within each heat exchanger and its logarithmic mean temperature difference (LMTD) as [55]

$$(UA) = \sum_{j=1}^{N} \frac{\left(\dot{E}/N\right)}{\Delta T_{LMTD,j}}. \quad (10)$$

The air cooler cost is estimated based on the thermal power exchanged $\left(\dot{E}_{Co}\right)$, which is also determined by the mass flow rate through and the inlet-outlet enthalpy difference of the heat exchanger. The electric generator cost is estimated based on the electric power generated, which was set as ~10 MW.

Regarding the main heat supplying device, similar to Eq. (9), the solar field cost is obtained as

$$C_{SF} = C_{Site} + C_{Mirrors} + C_{Rec}. \quad (11)$$

Both the site preparation and the mirrors costs are estimated based on the aperture area, which is simply obtained from the reference area and the solar multiple – as indicated in Eq. (5) –, whereas the receivers cost depends on their tube external area. Given the current non-availability of specific costs data for solar trough collectors operating with s-CO_2, costs for a solar tower collector were employed as a compromise scaling.

Table 1
TES length (L_{TES}) in m] based on the discharging time (t_{TES}) TES diameter (D_{TES}), and number of TES (N_{TES}).

$N_{TES} = 5$							
D_{TES} [m]	$t_{TES} = 0.25$ h	0.5 h	1 h	2 h	4 h	6 h	8 h
2.0	4.01	8.03	16.05	32.10	64.21	96.31	–
3.0	1.78	3.57	7.13	14.27	28.54	42.81	57.08
4.0	1.00	2.01	4.01	8.03	16.05	24.08	32.10
5.0	0.64	1.28	2.57	5.14	10.27	15.41	20.55

$N_{TES} = 10$							
D_{TES} [m]	$t_{TES} = 0.25$ h	0.5 h	1 h	2 h	4 h	6 h	8 h
1.5	3.57	7.13	14.27	28.54	57.08	85.61	114.15
2.0	2.01	4.01	8.03	16.05	32.10	48.16	64.21
3.0	0.89	1.78	3.57	7.13	14.27	21.40	28.54
4.0	0.50	1.00	2.01	4.01	8.03	12.04	16.05

$N_{TES} = 15$							
D_{TES} [m]	$t_{TES} = 0.25$ h	0.5 h	1 h	2 h	4 h	6 h	8 h
1.5	2.38	4.76	9.51	19.03	38.05	57.08	76.10
2.0	1.34	2.68	5.35	10.70	21.40	32.10	42.81
3.0	0.59	1.19	2.38	4.76	9.51	14.27	19.03
4.0	0.33	0.69	1.34	2.68	5.35	8.03	10.70

Table 2
Equipment cost expressions for the solar field and power block.

Equipment	Cost expression* [US$]
Turbine [53]	$9923.7\dot{W}^{0.5886}$
Compressor [53]	$643.15\dot{W}^{0.9142}$
Recuperator [53]	$5.2(UA)^{0.8933}$
Air cooler [54]	$1100\left(177.03\dot{E}_{Co} - \frac{\dot{E}_{Co}^2}{10^3} + \frac{\dot{E}_{Co}^3}{10^8}\right)$
Electric generator [54]	$6{\cdot}10^6\left(\frac{\dot{W}_{Ele}}{160}\right)^{0.7}$
Site preparation [54]	$20A_{Aper}$
Mirrors [54]	$120A_{Aper}$
Receivers [54]	$140{\cdot}10^6\left(\frac{A_{Rec}}{1571}\right)^{0.7}$

* $[\dot{W}]$ = kW, [UA] = W/K, $[\dot{E}_{Co}]$ = MW, $[\dot{W}_{Ele}]$ = MW, $[A_{Aper}] = [A_{Rec}]$ = m^2.

On the other hand, for the packed-bed TES system, the cost estimative relies on a different approach since parameters for scaling this component are still somewhat unknown. Such an approach relies on assuming the major costs of the packed-be TES device to be related to the pressure vessel [18] and the alumina particles. In this sense, the steel cost may be estimated as

$$C_{TES,st} = b_{st}\rho_{st}\left(V_{TES,Wall,st} + 2V_{TES,Lid,st}\right), \tag{12}$$

for which the TES steel wall and lid volumes are defined as

$$\begin{aligned} V_{TES,Wall,st} &= \frac{\pi}{4}\left[\left(D_{TES} + 2t_i + 2t_{st}\right)^2 - \left(D_{TES} + 2t_i\right)^2\right]L_{TES} \\ V_{TES,Lid,st} &= \frac{\pi}{4}D_{TES}^2 t_{st} \end{aligned}. \tag{13}$$

and $b_{st} = 1.553$ US$/kg is the steel specific cost, which was obtained as the average of the global composite prices for carbon steel and stainless steel 304 from Ref. [56], from January to August of 2019. Moreover, to bear the s-CO_2 pressure, the steel wall thickness is given by [57]

$$t_{st} = \frac{P_{PB}^{High}\left(D_{TES} + 2t_i\right)}{2\left(\sigma_{st} - 0.6P_{PB}^{High}\right)}, \tag{14}$$

for which P_{PB}^{High} is the high-temperature-end pressure and $t_i = 0.2$ m is the insulation thickness. Considering steel as the commercial reference material for pressure vessels and not accounting for any other possible mechanical improvements (i.e., the worst-case scenario), $\sigma_{st} = 140$ MPa corresponds to the adjusted material tensile strength for high working temperatures with a safety factor [34]. Within the limit values of 1.5 m and 4.0 m for D_{TES} in Table 1, t_{st} varies linearly from 0.19 m to 0.44 m. From a technical standpoint, and regarding novel under-development materials, using steel may not appear as the most reasonable option. Despite the expected increased and uncertain costs of such materials, they should offer a higher tensile strength, which leads to thinner walls. Thus, the adopted approach compensates for the non-ideal material by increasing the wall thickness.

For the alumina, similar to for the steel, the cost is estimated as

$$C_{TES,S} = b_S\rho_S(1-\varepsilon)V_{TES}, \tag{15}$$

where V_{TES} is the TES total internal volume and $b_S = 1.15$ US$/kg is the alumina specific cost, which was obtained based on the range of 1.0 US $/kg and 1.3 US$/kg for ceramic particles indicated by Ref. [53]. Therefore, the total cost for the TES system is obtained as

$$C_{TES} = N_{TES}\left(C_{TES,st} + C_{TES,S}\right), \tag{16}$$

where N_{TES} accounts for the number of TES devices employed.

Thus, from Eqs. (9), (11), and (15), the overall equipment investment cost is estimated as

$$C_{Equip} = C_{PB} + C_{SF} + C_{TES}, \tag{17}$$

which disregards any equipment cost related to the auxiliary heat exchanger discussed in Section 2.1.

For the auxiliary heating, which was adopted as using natural gas as fuel, the cost is estimated based on the specific fuel cost as

$$C_{Aux} = b_{Aux}E_{Aux}, \tag{18}$$

where $b_{Aux} = b_{NG} = 3.5 \cdot 10^{-9}$ US$/J is the specific cost of the auxiliary heating fuel, which was obtained as the average value for California/USA considering the available data for the last 10 years from Ref. [58] – it was considered that the energy of 1 $ft_{NG}^3 \approx 1030$ Btu = 1.0867 MJ [59]. Also, E_{Aux} accounts for the annual overall summation of energy obtained from the auxiliary heating, which is determined as

$$E_{Aux} = E_{Aux}^{PB} + E_{Aux}^{TES}, \tag{19}$$

where the auxiliary heating energy spent with the power block inlet (E_{Aux}^{PB}) and with the TES outlet (E_{TES}^{PB}) are obtained from summations throughout the 8760 h of the year as

$$E_{Aux}^{PB} = \sum_{j=1}^{8760}\dot{m}_{PB}\left(i_{F,PB}^{In} - i_{F,Aux,j}^{In}\right)\Delta t_{Sys}, \tag{20}$$

and

$$E_{Aux}^{TES} = N_{TES}\sum_{j=1}^{8760}\begin{cases} \langle\dot{m}_{TES,C}\rangle_j\left(i_{F,PB}^{Out} - \langle i_{F,TES,C}^{Out}\rangle_j\right)\Delta t_{Sys}, T_{TES,C}^{Out} < T_{PB}^{Out} \\ 0, T_{TES,C}^{Out} \geq T_{PB}^{Out} \end{cases}. \tag{21}$$

Also, the auxiliary heater inlet mass-specific enthalpy $i_{F,Aux}^{In}$ is obtained, for each system time step j, from the thermal balance from the solar field and TES outlets and the bypass as

$$\dot{m}_{SF}i_{F,SF}^{Out} + N_{TES}\langle\dot{m}_{TES}\rangle\langle i_{F,TES}^{Out}\rangle + \dot{m}_{Bypass}i_{F,PB}^{Out} = \dot{m}_{PB}i_{F,Aux}^{In}. \tag{22}$$

The environmental cost associated with the emission of CO_2 due to the use of auxiliary heating is also accounted for. Considering a lower heating value (LHV) of $LHV_{NG} = 45.5895$ MJ/kg [60] for the natural gas and that, from stoichiometry, the complete combustion of 1 kg of natural gas produces 2.75 kg of CO_2, the environmental cost is estimated as

$$C_{Env} = b_{Env}\frac{2.75E_{Aux}}{LHV}, \tag{23}$$

where $b_{Env} = 90 \cdot 10^{-3}$ US$/kg [61] is the environmental specific cost for the CO_2 emitted, i.e., taxation regarding the reduction of greenhouse emissions. It is worth mentioning that a future sensitivity analysis regarding such a value is recommended.

Furthermore, considering the difficulty of estimating the maintenance and operation costs, following Ref. [54], these were estimated as

$$C_{MO} = b_{MO}W_{PB,Net}, \tag{24}$$

where $W_{PB,Net}$, the net energy produced by the power block, is obtained from

$$W_{PB,Net} = \sum_{j=1}^{8760}W_{PB,j}^{Net}\Delta t_{Sys}, \tag{25}$$

and $b_{MO} = 3.5$ US$/MWh [54].

Therefore, as the figure of merit to evaluate the costs of energy production over the system lifetime, the economic analysis uses the levelized cost of energy (LCOE) approach [62], for which the $LCOE$ in US $/MWh is given by

$$LCOE = 3.6{\cdot}10^9\frac{\left[C_{Equip} + \sum_{j=1}^{LT}\frac{\left(C_{Aux,j} + C_{Env,j} + C_{MO,j}\right)}{(1+dr)^j}\right]}{\left[\sum_{j=1}^{LT}\frac{W_{Sys,Net,j}}{(1+dr)^j}\right]}, \tag{26}$$

considering, for a given year j within the system LT years lifetime, all costs described above to produce the annual system net energy $W_{Sys,Net,j}$, which is obtained as

$$W_{Sys,Net} = W_{PB,Net} - \sum_{j=1}^{8760}\dot{W}_{TES,j}^{Pump}\Delta t_{Sys}, \tag{27}$$

i.e., by subtracting from the annual net energy produced by the power block – considering that $\dot{W}_{PB}^{Net} = 9.93$ MW ≈ 10 MW is constant throughout the year – the annual energy expenditure with the TES auxiliary compressors, whose individual power consumption is expressed by [63]

$$\dot{W}^{Pump} = \left(\frac{1}{\eta_{Comp}}\right)\sum_{j=1}^{N_Z}\left[\left(\frac{\dot{m}_{F,w}+\dot{m}_{F,e}}{2}\right)\left(\frac{P_{F,w}-P_{F,e}}{\rho_{F,P}}\right)\right]. \quad (28)$$

Also, for all analyses, following Ref. [64], a lifetime of $LT = 20$ years and an annual discount rate of $dr = 5\%$ were considered.

Finally, it is important to mention that the adopted cost estimation methodology and reference values are not specific for the HTF considered. Therefore, it is expected, based on the available literature, accuracy of results roughly limited to a ±30% range [54,64].

3. Results and discussion

The following subsections present the results obtained and their discussions. Section 3.1 analyzes parametrically the system's economic behavior concerning the independent variables. Section 3.2 presents the economic-environmental assessment of the power plant. Then, Section 3.3 discusses the system's economic sensitivity to specific costs and TMY data.

3.1. Parametric analysis

For the economic assessment, first, the influence of the size of the TES system is examined in Fig. 6. Such a figure shows the integrated system *LCOE* variation with the design discharging time t_{TES} while considering three TES diameters, a solar multiple of $SM = 2$, and $N_{TES} = 5$ TES packed-bed devices. Additionally, the dash-dotted line indicates the *LCOE* value if no TES system is considered, which is referred to as the reference *LCOE* value. Regarding the configurations with an embedded TES (solid lines), one may notice that none achieved a lower *LCOE* than the reference. Furthermore, the rightmost portion of Fig. 6 reveals that a larger D_{TES} is preferable for smaller t_{TES} values, whereas the leftmost portion, which is zoomed in the detailed plot, shows that there is a swap between the preferable D_{TES} as t_{TES} decreases.

It should be mentioned that the convergence for the reference *LCOE* value as $t_{TES} \to 0$ is not observed. This convergence may be expected because the system response for ever-decreasing TES sizes approaches that of the system without any TES device and also because the associated cost should approach zero. Nevertheless, although for a given D_{TES}, $L_{TES} \to 0$ as $t_{TES} \to 0$ [34], the associated steel cost for the TES lids does not depend on L_{TES} (as is the case for the associated steel cost for the TES wall), but only on D_{TES}. Thus, this discussion clarifies the non-convergence of the *LCOE* curves for different D_{TES} as $t_{TES} \to 0$.

To account for the effects of the solar field size, which is expressed in terms of the solar multiple *SM*, on the levelized cost of energy, Fig. 7 shows the *LCOE* variation for five design discharging times t_{TES}, considering a TES diameter of $D_{TES} = 2$ m and $N_{TES} = 5$. Once again, the dash-dotted line indicates the reference *LCOE* values for each *SM* if no TES system is considered. The main point to be observed is the existence of local minima, i.e., for each t_{TES}, there is an *SM* minimizing the *LCOE*. Moreover, the optimal *SM* values decrease from roughly 3.5 to 2.0 as t_{TES} decreases from 8 h to the reference line (i.e., 0 h). This optimal trend is arguably related to matching the sizes of the solar field and TES systems. Furthermore, as shown in Fig. 6, the greater the TES size (i.e., its storage capacity), the greater the *LCOE*.

Furthermore, although the number of TES devices showed a minor influence on the *LCOE* when considering $N_{TES} = 10$ for longer discharging times, the variation within the range of $N_{TES} = 5$ and $N_{TES} = 15$ is arguably insignificant.

3.2. Economic-environmental assessment

As discussed in Section 3.1, the solutions with packed-bed TES systems did not present substantial improvements compared to their respective references if focusing exclusively on the *LCOE*. Moreover, the *LCOE* already accounts for the environmental-related economic cost of CO_2 emissions through specific taxation. Nonetheless, accounting for the monetary cost does not reduce the importance of reducing the actual environmental footprint. Hence, it is arguably reasonable to seek a compromise solution that minimizes the *LCOE* while also regards sustainability.

Considering the annual CO_2 mass emitted by the auxiliary heating (m_{CO2}) as a second independent figure of merit, Fig. 8a shows with black markers the values of *LCOE* (y-axis) and m_{CO2} (x-axis) for 140 combinations of *SM*, N_{TES}, t_{TES}, and D_{TES} – whose ranges are, respectively, 1.5 and 4.0, 0 and 15, 0 h and 8 h, and 1.5 m and 5 m. Both figures of merit, i.e., *LCOE* and m_{CO2}, were normalized by the maximal and minimal values of each for the set of combinations considered as

$$\varphi^* = \frac{\varphi - \varphi_{Min}}{\varphi_{Max} - \varphi_{Min}}, \quad (29)$$

while using, for the *LCOE*, the values 75.30 US$/MWh and 94.64 US $/MWh; whereas, for the m_{CO2}, the values $19.36 \cdot 10^6$ kg and $32.15 \cdot 10^6$ kg.

It is somewhat expected a competing effect (i.e., trade-off) between *LCOE* and m_{CO2}, i.e., the cleaner the solution, the greater the associated cost. Such a trend is visible in Fig. 8a, especially in its left lower quadrant, which suggests the possibility of using an optimization-based

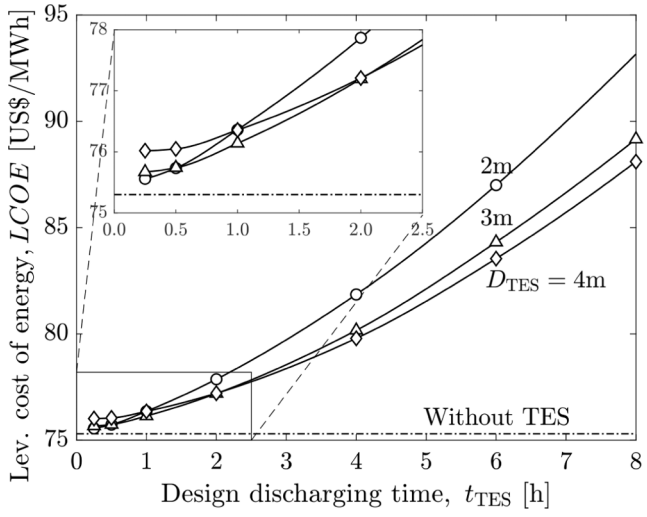

Fig. 6. *LCOE* variation with t_{TES} for fixed TES diameters of 2 m, 3 m, and 4 m while considering $SM = 2$ and $N_{TES} = 5$.

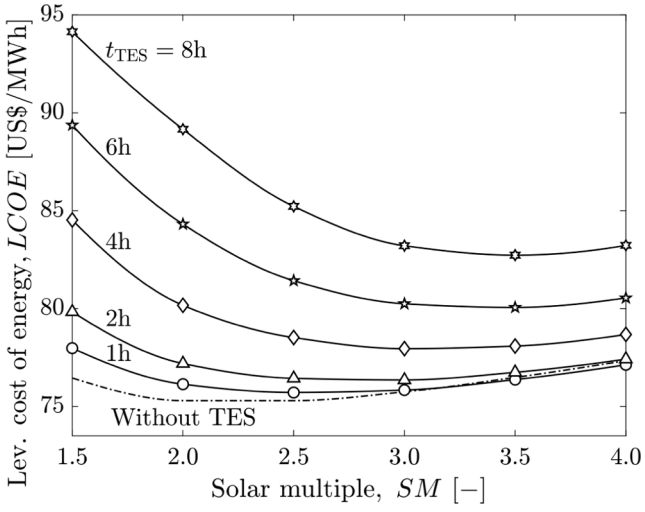

Fig. 7. *LCOE* variation with *SM* for fixed t_{TES} values of 1 h, 2 h, 4 h, 6 h, and 8 h while considering $N_{TES} = 5$ and $D_{TES} = 2$ m.

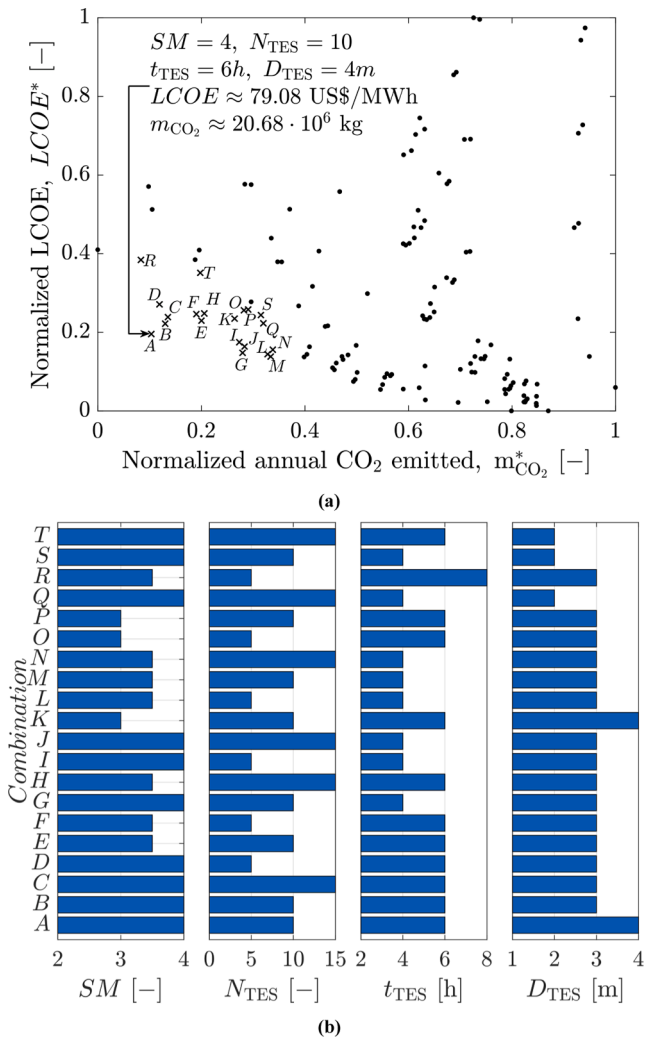

Fig. 8. (a) Normalized *LCOE* versus normalized annual m_{CO2} considering several combinations of *SM*, N_{TES}, t_{TES}, and D_{TES}; (b) Values of *SM*, N_{TES}, t_{TES}, and D_{TES} for the 20 best combinations of Fig. 8a.

approach for finding the Pareto front. Then, considering even weights to both figures of merit, the distance Γ of each point to the origin was simply evaluated as

$$\Gamma = \sqrt{(LCOE^*)^2 + (m^*_{CO2})^2}. \quad (30)$$

Thus, the 20 best out of the 140 evaluated combinations (i.e., those with smaller Γ) are indicated in Fig. 8a by the × markers and named alphabetically according to the increasing distance to the origin while the remaining combinations are indicated by the dot markers. The best compromise solution, i.e., point "A", was obtained with the combination $SM = 4$, $N_{TES} = 10$, $t_{TES} = 6$ h, and $D_{TES} = 4$ m and achieved $LCOE =$ 79.08 US$/MWh and $m_{CO2} = 20.68 \cdot 10^6$ kg.

Focusing on the aforementioned 20 best combinations and aiming to clarify the components of each one, Fig. 8b shows the values of *SM*, N_{TES}, t_{TES}, and D_{TES} for each of those cases. It is possible to verify that, for these combinations, none was obtained with an *SM* value smaller than 3.0, which indicates that an arguably larger solar field is preferred. Also, regarding the TES system, it is not possible to infer any clear tendency regarding the number of devices – which agrees with the discussion at the end of Section 3.1. Moreover, on the design discharging time (which is directly related to the TES volume), the best combinations were obtained with at least 4 h, which is roughly half of the range considered; then, it is conceivable that small TES systems do not play a significant role. Finally, regarding the D_{TES} parameter, there seems to be a preferable geometry with 75% of the combinations indicating a TES diameter of 3 m.

Now, Fig. 9a breaks down the *LCOE* of the aforementioned 20 best combinations into percentage components, which are sorted according to the *LCOE*. First, with regard to the percentage costs, one may check that there is a somewhat direct correlation between *LCOE* and the percentage C_{Equip} – a specific discussion on the equipment cost will be presented next. Then, it is also possible to verify a fairly inverse correlation between *LCOE* and the combined percentage $C_{Aux} + C_{Env}$. Following, the percentage C_{MO} remained nearly constant for all the 20 best combinations. Moreover, the last column on the RHS of Fig. 9a brings the total emitted mass of CO_2, whose tendency follows that of the combined $C_{Aux} + C_{Env}$, which is something expected because m_{CO2}, C_{Aux}, and C_{Env} are all directly dependent on E_{Aux} (see Eqs. (18) and (23). Also, yet on the combined $C_{Aux} + C_{Env}$, given the values adopted for b_{Aux}, b_{Env}, and *LHV*, it is possible to infer that this summation is dominated by the environmental taxation, which represents roughly 60% of the total amount, against the remaining roughly 40% due to the fuel cost. Furthermore, the competing effect between *LCOE* and m_{CO2} discussed in Fig. 8a becomes even clearer when comparing the first and last columns of Fig. 9a.

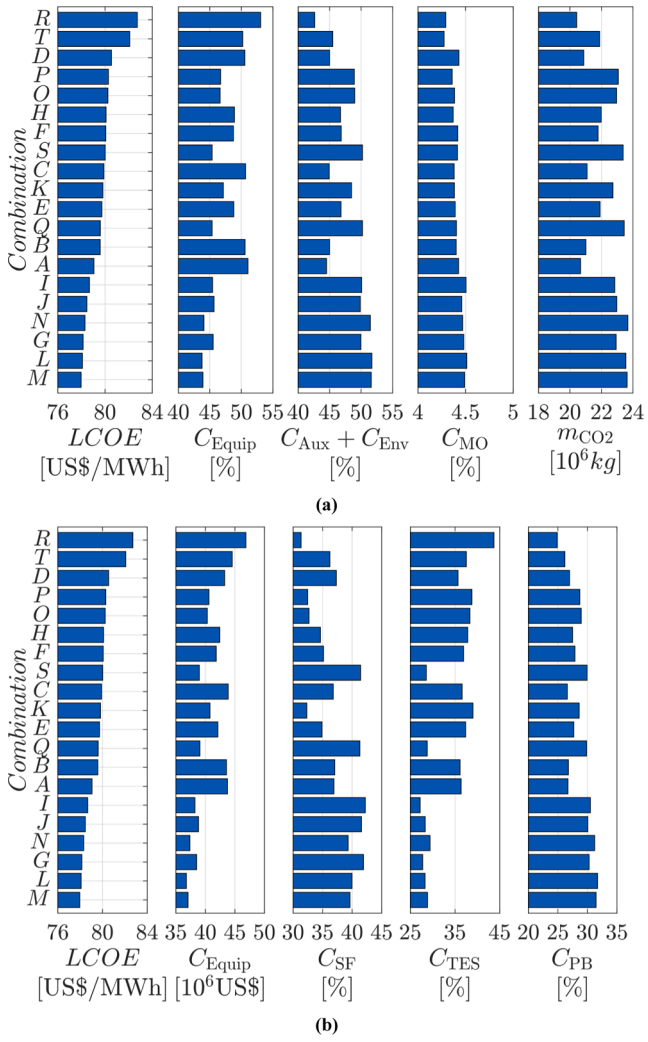

Fig. 9. (a) *LCOE*, its percentage breakdown into components, and m_{CO2} for the 20 best combinations of Fig. 8a (combinations are sorted according to their *LCOE* values; (b) *LCOE*, total equipment cost and its breakdown into components for the 20 best combinations of Fig. 8a (combinations are sorted according to their *LCOE* values).

Considering the equipment cost, Fig. 9b shows, once again, the 20 best combinations sorted according to their *LCOE*, but now it brings the total equipment cost and its percentage breakdown into the solar field (C_{SF}), thermal energy storage (C_{TES}), and power block (C_{PB}). It is possible to observe that the increase of the total equipment cost for the 20 best combinations is mostly driven by the TES cost, given that both the percentage C_{SF} and C_{PB} decrease as the *LCOE* increases. This analysis indicates the importance of investigating better and cost-effective materials for the TES construction.

3.3. Performance sensitivity analysis

Up to this point, the analyses considered fixed values for the specific costs. Because they depend on several factors, such as resource availability, environmental policies, market oscillations, it is important to verify the sensitivity of the results with respect to variations of those specific costs. Then, first focusing on the TES device, Fig. 10a shows the variation of the *LCOE* for the best compromise solution of Fig. 8a. For obtaining Fig. 10a, the values of the specific costs of alumina b_S and steel b_{st} varied within −50% and +50% with respect to standard values adopted. The *LCOE* for each combination was recalculated using the modified specific costs and is expressed in terms of percentage difference with respect to the baseline case – i.e., the *LCOE* = 79.08 US$/MWh from Fig. 8a, which is indicated by the black circle marker. As expected, the smallest value in Fig. 10a is obtained when both specific costs are decreased by half, whereas the largest when they are increased by half. Also, within the ranges considered, the variation of the *LCOE* is between roughly ±10%. Based on the tilt of the black dashed lines, which indicate constant values of *LCOE*, it is possible to infer that the figure of merit is more strongly influenced by b_{st} than by b_S.

Similar to Fig. 10a, Fig. 10b presents the variation of the *LCOE* focusing on the auxiliary heating needs, i.e., it shows the influence of varying the specific costs of the environmental taxation b_{Env} and auxiliary heating b_{Aux}. While b_{Aux} also varies from −50% to +50%, the range for b_{Env} was considered from −100% to +100%, which aims to consider non-uniform local environmental policies, i.e., such a range enables cases when no environmental taxation is applied and when an even heavier taxation is considered. By comparing Fig. 10b with Fig. 10a, it becomes clear that the auxiliary heating presents a stronger influence on the *LCOE* than the TES device, a conclusion that agrees with the discussion of Fig. 9a. For instance, with an equal variation of +50% for b_S and b_{st} in Fig. 10a and for b_{Env} and b_{Aux} in Fig. 10b, the the *LCOE* increased ∼22% for the latter and ∼10% for the former. Also, again from the tilt of the black dashed lines, it is possible to infer that the figure of merit is more strongly influenced by b_{Env} than by b_{Aux}.

Given that Fig. 10a only focused on the equipment cost of the TES system, Fig. 10c now complements the analysis by exploring the influence of varying the overall costs of the solar field and the power block. For both parameters, the variation considered a range of −50% to +50%. The results show that the effect on the *LCOE* of varying C_{PB} is ∼70% of that of varying C_{SF} by the same amount. Also, with an equal variation of +50% for both parameters, the LCOE increased ∼16%.

Similar to the specific costs, up to now, all analyses considered only the TMY meteorological conditions for Dagget/USA. Then, it is important to investigate the influence of meteorological data on the performance of the power plant. Based on favorable solar characteristics, the analysis gathered TMY data from seven more cities with prospects for developing CSP projects regarding Ref. [65]. For each new location considered, the Electronic Supplementary Material provides the meteorological data from Ref. [49] graphically, similar to Fig. 5.

For focusing on the effect of the meteorological input data, the analysis uses, once again, the fixed baseline values for the specific costs. The simulations for each TMY data set adopted a fixed number of TES devices of N_{TES} = 10 and a discharging time of t_{TES} = 6 h, whereas the solar multiples *SM* of 2.0, 3.0, and 4.0 and TES diameters D_{TES} of 2.0 m, 3.0 m, and 4.0 m. The reason for fixing N_{TES} is its non-important influence on the result, as previously discussed at the end of Section 3.1. Now, regarding t_{TES}, apart from being a common practice to define a design discharging time, fixing such a parameter enables fair comparisons. Additionally, the simulations also considered the solutions without a TES system for each *SM* value and TMY data.

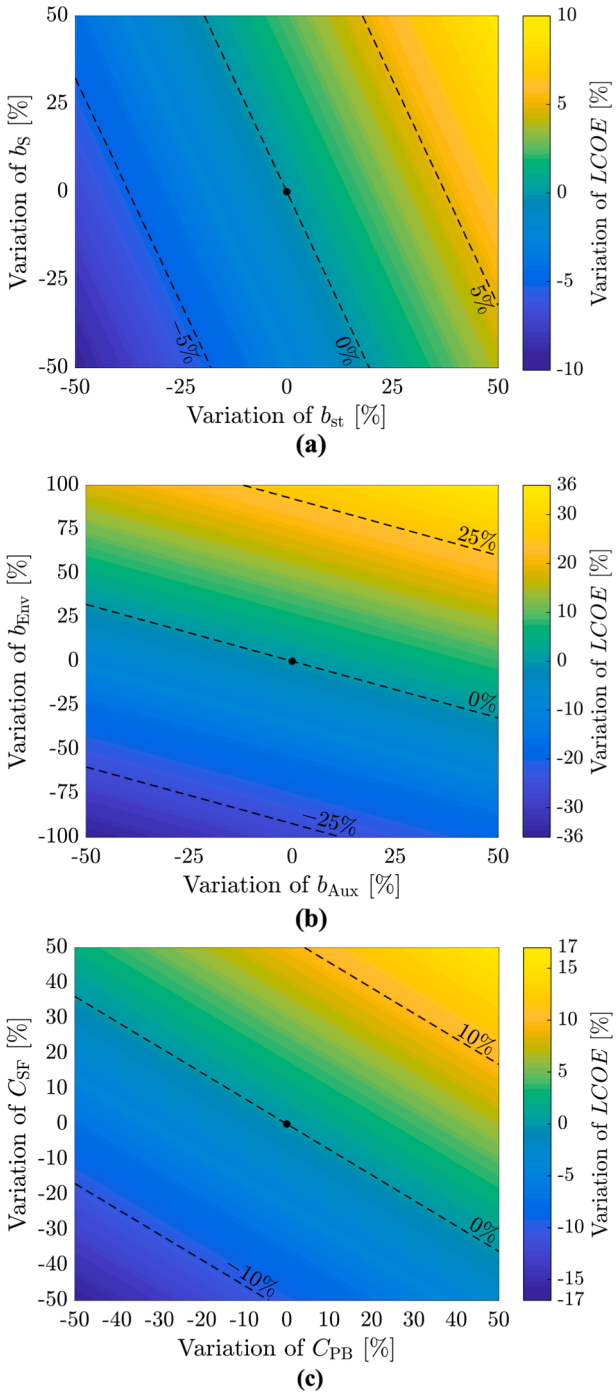

Fig. 10. Sensitivity of *LCOE* for the best combination of Fig. 8a with respect to (a) the specific costs of the TES device, i.e., the steel cost b_{st} and porous medium material b_S; (b) the auxiliary heating, i.e., the fuel cost b_{Aux} and environmental taxation b_{Env}; (c) the equipment costs for the solar field C_{SF} and the power block C_{PB}.

To build Fig. 11, besides (1) Dagget/USA, the other TMY data refer to (2) Medicine Hat/Canada, (3) Antofagasta/Chile, (4) Casablanca/Morocco, (5) Sevilla/Spain, (6) Delingha/China, (7) Anantapur/India, and (8) Adelaide/Australia. This figure, similar to Fig. 8a, shows the

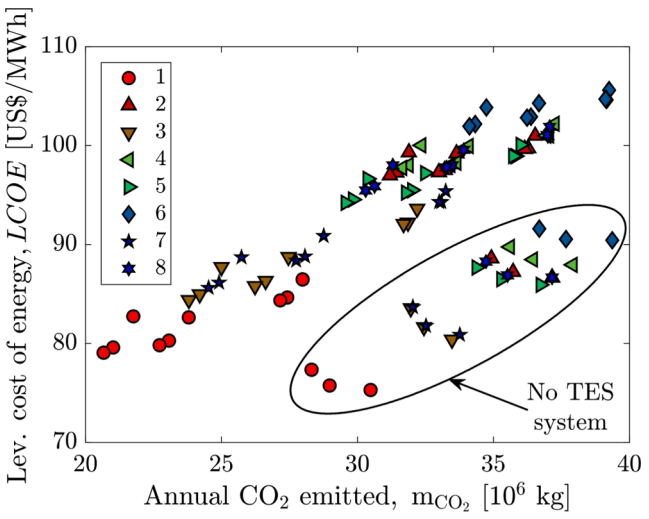

Fig. 11. *LCOE* versus annual m_{CO2} (with and without TES system) considering $N_{TES} = 10$, $t_{TES} = 6$ h, *SM* of 2.0, 3.0, and 4.0 and D_{TES} of 2.0 m, 3.0 m, and 4.0 m using the TMY data for: (1) Dagget/USA, (2) Medicine Hat/Canada, (3) Antofagasta/Chile, (4) Casablanca/Morocco, (5) Sevilla/Spain, (6) Delingha/China, (7) Anantapur/India, and (8) Adelaide/Australia.

LCOE versus the annual m_{CO2} for each combination, but it does not normalize the values for enabling direct comparisons. From that data obtained, it is clear that Dagget/USA remains the best compromise solution, followed by Antofagasta/Chile and Anantapur/India. The region in detail in the low-right quadrant exhibits the options without any TES system, i.e., those relying entirely on the auxiliary heater as backup. The variability of the results between locations with favorable meteorological characteristics for CSP applications points towards the necessity of additional optimization-oriented investigations. Although such detailed analyses escape the scope of the present work, it is worth mentioning that, apart from the required TMY data, they must use updated specific costs accounting for local characteristics.

4. Conclusions

This study economic and environmentally investigated an integrated s-CO_2 solar-powered plant composed of a solar field, packed-bed TES system, and power block. The annual transient simulations employed thoroughly detailed models and specific costs for subsystems. From the parametric analysis of the economic behavior of the integrated system, the results showed that (i) larger D_{TES} values are preferable for smaller t_{TES} values, whereas there is a swap between the preferable D_{TES} as t_{TES} decreases and (ii) the existence of local minima of *LCOE* for different t_{TES} with respect to *SM*, whose optimal trend is arguably related to matching the sizes of the solar field and TES systems.

Moreover, the trade-off assessment pointed towards a compromise solution concerning economic cost and environmental footprint, i.e., the combination $SM = 4$, $N_{TES} = 10$, $t_{TES} = 6$ h, and $D_{TES} = 4$ m, which achieved $LCOE = 79.08$ US$/MWh and $m_{CO2} = 20.68 \cdot 10^6$ kg. The analysis indicated the importance of investigating better and cost-effective materials for the construction of the TES system. Additionally, the sensitivity analysis of the system performance concerning the specific costs of the TES system and the auxiliary heating showed that the auxiliary heating presents a stronger influence on the *LCOE* than the TES device. Specifically, concerning the latter, the figure of merit is more sensitive to b_{st} than to b_S. Now, regarding the auxiliary heating, the figure of merit is more strongly influenced by b_{Env} than by b_{Aux}. Furthermore, on the sensitivity to the TMY data, the variability of the results requires considering updated local characteristics and further optimization-oriented investigations. Considering the uncertainties associated with the economic model, a possibly attractive option is associating the genetic algorithm with the Monte Carlo method.

Finally, this work may be considered an exploratory effort on assessing the feasibility of TES-aided solar-powered plants using s-CO_2. Although the solutions with packed-bed TES systems did not present substantial improvements in terms of *LCOE* by themselves compared to the respective references, the results revealed the possible feasibility of the s-CO_2 integrated system and evidenced several venues for further examination. Since several parameters substantially influence such an economic-environmental assessment, follow-up broader sensitivity analyses are highly recommended for exploring the influence of other parameters and figures of merit. Therefore, these analyses and discussions comprise a preliminary assessment for facilitating and encouraging further related developments.

CRediT authorship contribution statement

F.G. Battisti: Conceptualization, Methodology, Software, Validation, Formal analysis, Writing – original draft, Writing – review & editing. **L.A. de Araujo Passos:** Conceptualization, Methodology, Software, Validation, Formal analysis, Writing – review & editing. **A.K. da Silva:** Conceptualization, Methodology, Writing – review & editing.

Declaration of Competing Interest

The authors declare that they have no known competing financial interests or personal relationships that could have appeared to influence the work reported in this paper.

Acknowledgments

The support from Petrobras and ANEEL (PD-00553-0042/2016) is appreciated. This study was financed in part by the Conselho Nacional de Desenvolvimento Científico e Tecnológico – Brasil (CNPq). This study was financed in part by the Coordenação de Aperfeiçoamento de Pessoal de Nível Superior – Brasil (CAPES) – Finance Code 001. The first author also acknowledges the support from Petrobras/PFRH (6000.0062072.10.4), as well as ANP, FINEP, MCTI through PRH.

Appendix A

Following Ref. [34], for the porous medium of the packed-bed TES system, the general conservative form of the energy conservation equations are given by [34]

$$\frac{\partial(\rho i)}{\partial t} + \vec{\nabla}\cdot(\rho \vec{u} i) = \vec{\nabla}\cdot(k\vec{\nabla}T) + \frac{DP}{Dt}, \tag{A1}$$

and

$$\frac{\partial(\rho e)}{\partial t} = \vec{\nabla}\cdot(k\vec{\nabla}T), \tag{A2}$$

for the fluid (in terms of the mass-specific enthalpy i) and solid (in terms of the mass-specific energy e) phases, respectively. The packed-bed model uses the finite-volumes method and axial discretization to solve these equations. In the present work, for improving the stability of the numerical routine , a new approach couples the mass-specific enthalpy and temperature (T) of the fluid. By linearizing the mass-specific enthalpy as

$$i_F(T_F) \approx i_F\left(T_F = T_{F,a}\right) + \left(T_F - T_{F,a}\right)\left.\frac{\partial i_F}{\partial T_F}\right|_{T_F = T_{F,a}}, \tag{A3}$$

and using $\partial i_F/\partial T_F = c_F$, the expression for the temperature of the fluid becomes

$$T_F \approx T_{F,a} + \left[\frac{i_F(T_F) - i_F\left(T_{F,a}\right)}{c_F\left(T_{F,a}\right)}\right], \tag{A4}$$

for which c_F is taken as the mass-specific heat at constant pressure and the subscripts F and a denote fluid and approximated, respectively. This simple approach uses the previous iteration value as an approximation to update the temperature of the fluid through a somewhat correction factor. In addition, this method improves the convergence of the numerical routine. Such an improvement is due to the linearization providing better guesses for the subsequent iteration. Then, the discretized version of Eq. (A1) becomes

$$\left(-\dot{m}_{F,w}\right) i_{F,W} + \left[\frac{\varepsilon V_P \rho_{F,P}}{\Delta t} + \dot{m}_{F,e} + \frac{h_{v,P} V_P}{c_{F,P,a}} + \frac{h_{Wall,P} A_{Wall,P}}{c_{F,P,a}}\right] i_{F,P} + \left(-h_{v,P} V_P\right) T_{S,P} = \left(\frac{\varepsilon V_P \rho^0_{F,P} i^0_{F,P}}{\Delta t}\right) + h_{v,P} V_P \left(-T_{F,P,a} + \frac{i_{F,P,a}}{c_{F,P,a}}\right)$$
$$+ h_{Wall,P} A_{Wall,P} \left(T_{Wall,P} - T_{F,P,a} + \frac{i_{F,P,a}}{c_{F,P,a}}\right) + \varepsilon V_P \left(P_{F,P} - P^0_{F,P}\right) + \left(\frac{\dot{m}_{F,e}}{\rho_{F,e}}\right)\left(P_{F,e} - P_{F,P}\right) + \left(\frac{\dot{m}_{F,w}}{\rho_{F,w}}\right)\left(P_{F,P} - P_{F,w}\right). \tag{A5}$$

Similarly, the discretized expression of Eq. (A2) becomes

$$\left(-\frac{k_{S,eff,w} A_w}{\Delta z}\right) T_{S,W} + \left[\frac{(1-\varepsilon) V_P \rho_S \alpha_{1,P}}{\Delta t} + h_{v,P} V_P + \frac{k_{S,eff,w} A_w}{\Delta z} + \frac{k_{S,eff,e} A_w}{\Delta z}\right] T_{S,P} + \left(-\frac{k_{S,eff,e} A_e}{\Delta z}\right) T_{S,E} + \left(\frac{-h_{v,P} V_P}{c_{F,P,a}}\right) i_P$$
$$= \frac{(1-\varepsilon) V_P \rho_S \left(e^0_P - \alpha_{2,P}\right)}{\Delta t} + h_{v,P} V_P \left(T_{F,P,a} - \frac{i_{F,P,a}}{c_{F,P,a}}\right). \tag{A6}$$

In both expressions, $\dot{m}$ is the total mass flow rate through the packed bed, V the node total volume, h the convective heat transfer coefficient, ρ the volume-specific mass, t the time, P the thermodynamic pressure, h_v the volumetric convective heat transfer coefficient, k the thermal conductivity, A the total transversal area, and α_j the solid mass-specific internal energy linearization factors. The subscripts S, eff, and $Wall$ refer to solid, effective, and wall, respectively. The superscript 0 refers to the previous time step, whereas no superscript, the current time step. Also, the subscripts W, P, and E refer to west, current, and east, respectively, with the upper case indicating a node and lower case a boundary. For the complete packed-bed modeling, see Ref. [34].

For the sake of clarity, it is essential to justify the assumption $\partial i_F/\partial T_F = c_F$. From thermodynamics, it is possible to express a variation of the mass-specific enthalpy as

$$di = \left.\frac{\partial i}{\partial T}\right|_P dT + \left.\frac{\partial i}{\partial P}\right|_T dP. \tag{A7}$$

Then, from the definition of the mass-specific heat as constant pressure, i.e.,

$$c = \left.\frac{\partial i}{\partial T}\right|_P, \tag{A8}$$

it is possible to rewrite Eq. (A7) as

$$di = cdT + \left.\frac{\partial i}{\partial P}\right|_T dP. \tag{A9}$$

Because, during an iteration of the packed-bed routine, the numerical process for obtaining the new distributions of mass-specific enthalpy of the fluid and temperature of the solid considers a fixed pressure field, the pressure variation in Eq. (A9) is null. Specifically, within an iteration, after solving the distributions mentioned above, as already discussed, the routine updates the pressure. Hence, Eq. (A5) indicates the reasonableness of the assumption $\partial i_F/\partial T_F = c_F$ used in the linearization of Eq. (A3).

Appendix B

When the TES device idles, Ref. [34] numerically finds the equilibrium pressure at each time step, i.e., the value of the pressure that maintains constant the total mass within the TES vessel. Such a process is very time consuming because it relies on finding the zero of an equation that depends on updated thermophysical properties. Then, for diminishing the run time of the algorithm, an alternative process was used. From the thermodynamics, it is possible to express a variation of the volume-specific mass as

$$d\rho = \left.\frac{\partial \rho}{\partial T}\right|_P dT + \left.\frac{\partial \rho}{\partial P}\right|_T dP. \tag{B1}$$

Also, using the isobaric expansion coefficient (β) and the isothermal compressibility coefficient (κ), which are defined as

$$\begin{aligned}\beta &\equiv \frac{1}{v}\frac{\partial v}{\partial T}\bigg|_P = \left(-\frac{1}{\rho}\right)\frac{\partial \rho}{\partial T}\bigg|_P \\ \kappa &\equiv \left(-\frac{1}{v}\right)\frac{\partial v}{\partial P}\bigg|_T = \left(\frac{1}{\rho}\right)\frac{\partial \rho}{\partial P}\bigg|_T\end{aligned}, \tag{B2}$$

it is possible to rewrite Eq. (B1) as

$$\frac{d\rho}{\rho} = -\beta dT + \kappa dP. \tag{B3}$$

Similar to other thermodynamic properties, both β and κ are easily obtained from CoolProp [36,37]. Then, integrating both sides of Eq. (B3) over a generic thermodynamic process, it becomes

$$\ln\left(\frac{\rho}{\rho^0}\right) = -\beta^{i-1}\left(T - T^0\right) + \kappa^{i-1}\left(P - P^0\right), \tag{B4}$$

for which (i) the superscript 0 indicates the previous state (i.e., previous time step) and the lack of such a superscript indicates the current state (i.e., current time step) and (ii) the superscript i-1 indicates the evaluation at a previous iteration and the lack of such a superscript indicates evaluation at the current iteration. So, Eq. (B4) may be rewritten as

$$\rho = \rho^0\left[\frac{\exp\left[\kappa^{i-1}\left(P - P^0\right)\right]}{\exp\left[\beta^{i-1}\left(T - T^0\right)\right]}\right]. \tag{B5}$$

Now, considering that while the fixed-volume TES device idles, the fluid mass within it at the end of the discharge (M) remains constant and that the pressure at a given time step for all of the axial nodes j is uniform, i.e., $P_j = P$, it is possible to express such a fluid mass as

$$M = \sum_{j=1}^{N_z}\left(V_j\varepsilon\rho_j\right) = \sum_{j=1}^{N_z}\left\{V_j\varepsilon\rho_j^0\frac{\exp\left[\kappa_j^{i-1}\left(P - P_j^0\right)\right]}{\exp\left[\beta_j^{i-1}\left(T_j - T_j^0\right)\right]}\right\}. \tag{B6}$$

Focusing on the term containing the pressure P, following Eq. (A1), one may linearize such a term as

$$\exp\left[\kappa_j^{i-1}\left(P - P_j^0\right)\right] \approx \exp\left[\kappa_j^{i-1}\left(P_j^{i-1} - P_j^0\right)\right] + \left(P - P_j^{i-1}\right)\kappa_j^{i-1}\exp\left[\kappa_j^{i-1}\left(P_j^{i-1} - P_j^0\right)\right] \tag{B7}$$

Then, using Eq. (B7), Eq. (B6) may be rewritten as

$$M - \sum_{j=1}^{N_z}\left\{\frac{V_j\varepsilon\rho_j^0\exp\left[\kappa_j^{i-1}\left(P_j^{i-1} - P_j^0\right)\right]}{\exp\left[\beta_j^{i-1}\left(T_j - T_j^0\right)\right]}\left(1 + \kappa_j^{i-1}P - \kappa_j^{i-1}P^{i-1}\right)\right\} = 0. \tag{B8}$$

Finally, because the equilibrium pressure is uniform and constant at a given time step, it is possible to express it as

$$P = \frac{M - \sum_{j=1}^{N_z}\left\{\frac{V_j\varepsilon\rho_j^0\left(1-\kappa_j^{i-1}P^{i-1}\right)\exp\left[\kappa_j^{i-1}\left(P_j^{i-1}-P_j^0\right)\right]}{\exp\left[\beta_j^{i-1}\left(T_j-T_j^0\right)\right]}\right\}}{\sum_{j=1}^{N_z}\left\{\frac{V_j\varepsilon\rho_j^0\kappa_j^0\exp\left[\kappa_j^{i-1}\left(P_j^{i-1}-P_j^0\right)\right]}{\exp\left[\beta_j^{i-1}\left(T_j-T_j^0\right)\right]}\right\}}. \tag{B9}$$

With Eq. (B9), the equilibrium pressure may be simply updated between iterations, without requiring a dedicated numerical solver.

Appendix C. Supplementary material

Supplementary data to this article can be found online at https://doi.org/10.1016/j.apenergy.2022.118913.

References

[1] Yan J, Yang X. Thermal energy storage: An overview of papers published in Applied Energy 2009–2018. Appl Energy 2021;285:116397.
[2] Olabi A, Abdelkareem M. Energy storage systems towards 2050. Energy 2021;219:119634.
[3] Pelay U, Luo L, Fan Y, Stitou D, Rood M. Thermal energy storage systems for concentrated solar power plants. Renew Sustain Energy Rev 2017;79:82–100.
[4] Achkari O, El Fadar A. Latest developments on TES and CSP technologies – Energy and environmental issues, applications and research trends. Appl Therm Eng 2020;167:114806.
[5] Awan AB, Khan MN, Zubair M, Bellos E. Commercial parabolic trough CSP plants: Research trends and technological advancements. Sol Energy 2020;211:1422–58.
[6] Zaharil HA. An investigation on the usage of different supercritical fluids in parabolic trough solar collector. Renew Energy 2021;168:676–91.
[7] Biencinto M, González L, Valenzuela L, Zarza E. A new concept of solar thermal power plants with large-aperture parabolic-trough collectors and sCO2 as working fluid. Energy Convers Manage 2019;199:112030.
[8] Ehsan MM, Guan Z, Gurgenci H, Klimenko A. Novel design measures for optimizing the yearlong performance of a concentrating solar thermal power plant using thermal storage and a dry-cooled supercritical CO2 power block. Energy Convers Manage 2020;216:112980.
[9] Crespi F, Gavagnin G, Sánchez D, Martínez GS. Supercritical carbon dioxide cycles for power generation: A review. Appl Energy 2017;195:152–83.
[10] Ahn Y, Bae SJ, Kim M, Cho SK, Baik S, Lee JI, et al. Review of supercritical CO2 power cycle technology and current status of research and development. Nucl Eng Technol 2015;47(6):647–61.
[11] Crespi F, Sánchez D, Rodríguez JM, Gavagnin G. A thermo-economic methodology to select sCO2 power cycles for CSP applications. Renew Energy 2020;147(Part 3):2905–12.
[12] Ma Y, Morosuk T, Luo J, Liu M, Liu J. Superstructure design and optimization on supercritical carbon dioxide cycle for application in concentrated solar power plant. Energy Convers Manage 2020;206:112290.
[13] Wang X, Li X, Li Q, Liu L, Liu C. Performance of a solar thermal power plant with direct air-cooled supercritical carbon dioxide Brayton cycle under off-design conditions. Appl Energy 2020;261:114359.

[14] Anderson MNGCM. Materials, Turbomachinery and Heat Exchangers for Supercritical CO2 Systems. Battelle Energy Alliance (Project Number: 09-778); 2012.
[15] Frazzica A, Cabeza LF. Recent Advancements in Materials and Systems for Thermal Energy Storage: An Introduction to Experimental Characterization Methods. Springer; 2018.
[16] Gasia J, Miró L, Cabeza LF. Review on system and materials requirements for high temperature thermal energy storage. Part 1: General requirements. Renew Sustain Energy Rev 2017;75:1320–38.
[17] Alva G, Liu L, Huang X, Fang G. Thermal energy storage materials and systems for solar energy applications. Renew Sustain Energy Rev 2017;68:693–706.
[18] Kelly B. Advanced Thermal Storage for Central Receivers with Supercritical Coolants. DE-FG36-08GO18149. Abengoa Solar Inc; 2010.
[19] Trevisan S, Guédez R, Laumert B. Supercritical CO2 Brayton Power Cycle for CSP With Packed Bed TES Integration and Cost Benchmark Evaluation. In: ASME Power Conference, vol. 59100, no. ASME Power Conference; 2019. p. V001T06A010.
[20] Trevisan S, Guédez R, Laumert B. Thermo-economic optimization of an air driven supercritical CO2 Brayton power cycle for concentrating solar power plant with packed bed thermal energy storage. Sol Energy 2020;211:1373–91.
[21] Johnson E, Bates L, Dower A, Bueno PC, Anderson R. Thermal energy storage with supercritical carbon dioxide in a packed bed: Modeling charge-discharge cycles. J Supercrit Fluids 2018;137:57–65.
[22] Osorio JD, Hovsapian R, Ordonez JC. Effect of multi-tank thermal energy storage, recuperator effectiveness, and solar receiver conductance on the performance of a concentrated solar supercritical CO2-based power plant operating under different seasonal conditions. Energy 2016;115:353–68.
[23] Osorio JD, Hovsapian R, Ordonez JC. Dynamic analysis of concentrated solar supercritical CO2-based power generation closed-loop cycle. Appl Therm Eng 2016;93:920–34.
[24] Liu J, Chen H, Xu Y, Wang L, Tan C. A solar energy storage and power generation system based on supercritical carbon dioxide. Renew Energy 2014;64:43–51.
[25] Zhu H-H, Wang K, He Y-L. Thermodynamic analysis and comparison for different direct-heated supercritical CO2 Brayton cycles integrated into a solar thermal power tower system. Energy 2017;140:144–57.
[26] de Araujo Passos LA, de Abreu SL, da Silva AK. A short- and long-term demand based analysis of a CO2 concentrated solar power system with backup heating. Appl Therm Eng 2019;160:1359–4311.
[27] Thanganadar D, Fornarelli F, Camporeale S, Asfand F, Patchigolla K. Off-design and annual performance analysis of supercritical carbon dioxide cycle with thermal storage for CSP application. Appl Energy 2021;282(Part A):116200.
[28] Battisti FG, Delsoto GS, da Silva AK. Transient analysis and optimization of a recuperative sCO2 Brayton cycle assisted by heat and mass storage systems. Energy 2018;150:979–91.
[29] Hobold GM, da Silva AK. Critical phenomena and their effect on thermal energy storage in supercritical fluids. Appl Energy 2017;205:1447–58.
[30] Liu Z, Liu Z, Xin X, Yang X. Proposal and assessment of a novel carbon dioxide energy storage system with electrical thermal storage and ejector condensing cycle: Energy and exergy analysis. Appl Energy 2020;269:115067.
[31] de la Calle A, Bayon A, Pye J. Techno-economic assessment of a high-efficiency, low-cost solar-thermal power system with sodium receiver, phase-change material storage, and supercritical CO2 recompression Brayton cycle. Sol Energy 2020;199:885–900.
[32] Neises T, Turchi C. Supercritical carbon dioxide power cycle design and configuration optimization to minimize levelized cost of energy of molten salt power towers operating at 650 °C. Sol Energy 2019;181:27–36.
[33] Liang Y, Chen J, Yang Z, Chen J, Luo X, Chen Y. Economic-environmental evaluation and multi-objective optimization of supercritical CO2 based-central tower concentrated solar power system with thermal storage. Energy Convers Manage 2021;238:114140.
[34] Battisti FG, de Araujo Passos LA, da Silva AK. Performance mapping of a packed-bed thermal energy storage for concentrating solar-powered plants using supercritical carbon dioxide. Appl Therm Eng 2021;183(1). https://doi.org/10.1016/j.applthermaleng.2020.116032.
[35] The MathWorks Inc., Matlab; 2017b.
[36] "CoolProp," [Online]. Available: http://www.coolprop.org [accessed 25 03 2019].
[37] Bell I, Wronski J, Quoilin S, Lemort V. Pure and pseudo-pure fluid thermophysical property evaluation and the open-source thermophysical property library CoolProp. Ind Eng Chem Res 2014;53:2498–508.
[38] Stein WH, Buck R. Advanced power cycles for concentrated solar power. Sol Energy 2017;152:91–105.
[39] Dunham MT, Iverson BD. High-efficiency thermodynamic power cycles for concentrated solar power systems. Renew Sustain Energy Rev 2014;30:758–70.
[40] Muñoz-Anton J, Biencinto M, Zarza E, Díez LE. Theoretical basis and experimental facility for parabolic trough collectors at high temperature using gas as heat transfer fluid. Appl Energy 2014;135:373–81.
[41] de Araujo Passos LA, de Abreu SL, da Silva AK. Time-dependent behavior of a recompression cycle with direct CO2 heating through a parabolic collector array. Appl Therm Eng 2018;140:593–603.
[42] Dyreby J. Modeling the Supercritical Carbon Dioxide Brayton Cycle with Recompression [Ph.D. Dissertation]. University of Wisconsin-Madison; 2014.
[43] Bahamonde Noriega J. Design method for s-CO2 gas turbine power plants: Integration of thermodynamic analysis and components design for advanced applications [Master Thesis]. Delft University of Technology; 2012.
[44] Gnielinski V. Heat transfer coefficients for turbulent flow in concentric annular ducts. Heat Transf Eng 2009;30(6):431–6.
[45] Luu MT, Milani D, McNaughton R, Abbas A. Dynamic modelling and start-up operation of a solar-assisted recompression supercritical CO2 Brayton power cycle. Appl Energy 2017;199:247–63.
[46] Singh R, Miller SA, Rowlands AS, Jacobs PA. Dynamic characteristics of a direct-heated supercritical carbon-dioxide Brayton cycle in a solar thermal power plant. Energy 2013;50:194–204.
[47] Linares JI, Montes MJ, Cantizano A, Sánchez C. A novel supercritical CO2 recompression Brayton power cycle for power tower concentrating solar plants. Appl Energy 2020;263.
[48] Forristall R. Heat transfer analysis and modeling of a parabolic trough solar receiver implemented in engineering equation solver. Golden, CO (US): National Renewable Energy Lab.; 2003.
[49] "EnergyPlus," [Online]. Available: https://energyplus.net/weather [accessed 20 August 2019].
[50] Buol S. Tropical soils| humid tropica. Elsevier; 2013.
[51] Bejan A, Tsatsaronis G, Moran M. Thermal Design and Optimization. John Wiley and Sons; 1996.
[52] Ahmadi P, Dincer I, Rosen MA. Exergy, exergoeconomic and environmental analyses and evolutionary algorithm based multi-objective optimization of combined cycle power plants. Energy 2011;36(10):5886–98.
[53] Ho CK, Carlson M, Garg P, Kumar P. Technoeconomic analysis of alternative solarized s-CO2 Brayton cycle configurations. J Sol Energy Eng 2016;138(5).
[54] Manzolini G, Binotti M, Bonalumi D, Invernizzi C, Iora P. CO2 mixtures as innovative working fluid in power cycles applied to solar plants. Techno-economic assessment. Sol Energy 2019;181:530–44.
[55] Nellis G, Klein S. Heat Transfer. New York: Cambridge University Press; 2009.
[56] "World Steel Prices," [Online]. Available: https://worldsteelprices.com/ [accessed 6 January 2020].
[57] ASME, "Power piping: ASME code for pressure piping, B31.1-2001," New York: ASME; 2002.
[58] "US Energy Information Administration," [Online]. Available: https://www.eia.gov/dnav/ng/hist/n3050ca3m.htm [accessed 10 January 2020].
[59] "IndexMundi," [Online]. Available: https://www.indexmundi.com/commodities/glossary/mmbtu [accessed 10 January 2020].
[60] "Sciencedirect," [Online]. Available: https://www.sciencedirect.com/topics/engineering/calorific-value [accessed 10 January 2020].
[61] Aminyavari M, Najafi B, Shirazi A, Rinaldi F. Exergetic, economic and environmental (3E) analyses, and multi-objective optimization of a Co2/NH3 cascade refrigeration system. Appl Therm Eng 2014;65(1–2):42–50.
[62] Dowling AW, Zheng T, Zavala VM. Economic assessment of concentrated solar power technologies: A review. Renew Sustain Energy Rev 2017;72:1019–32.
[63] Fox RW, McDonald AT, Pritchard PJ. Introduction to fluid mechanics. Hoboken, New Jersey: Wiley; 2003.
[64] Wright SA, Davidson CS, Scammell WO. Thermo-economic analysis of four sCO2 waste heat recovery power systems. In: Fifth International SCO2 Symposium, San Antonio, TX; 2016.
[65] "SolarPACES," [Online]. Available: https://solarpaces.nrel.gov/by-country [accessed 15 August 2019].